Title:

Dominant role of mineral dust in cirrus cloud formation revealed by global-scale measurements

Author list:

Karl D. Froyd[1,2*], Pengfei Yu[1,2,3], Gregory P. Schill[1,2], Charles A. Brock[1], Agnieszka Kupc[1,4], Christina J. Williamson[1,2], Eric J. Jensen[1,2], Eric Ray[1,2], Karen H. Rosenlof[1], Huisheng Bian[5,6], Anton S. Darmenov[5], Peter R. Colarco[5], Glenn S. Diskin[7], ThaoPaul Bui[8], and Daniel M. Murphy[1]

Affiliations:

[1]Chemical Sciences Laboratory, National Oceanic and Atmospheric Administration, Boulder, CO, USA.

[2]Cooperative Institute for Research in Environmental Sciences, University of Colorado, Boulder, CO, USA.

[3]Institute for Environment and Climate Research, Jinan University, Guangzhou, China.

[4]Faculty of Physics, Aerosol Physics and Environmental Physics, University of Vienna, Vienna, Austria.

[5]NASA Goddard Space Flight Center, Greenbelt, MD, USA.

[6]University of Maryland at Baltimore County, Baltimore County, MD, USA.

[7]NASA Langley Research Center, Hampton, VA, USA.

[8]NASA Ames Research Center, Moffett Field, CA, USA.

*Correspondence to: Karl.Froyd@colorado.edu

Abstract:

Airborne mineral dust particles can act as natural seeds for cirrus clouds in the upper troposphere. However, dust atmospheric abundance is unconstrained in cirrus-forming regions, hampering our ability to predict these radiatively important clouds. Here, we present global-scale measurements of dust aerosol abundance in the upper troposphere, and incorporate these into a detailed cirrus formation model. We show that dust aerosol initiates cirrus clouds throughout the extra-tropics in all seasons and dominates cirrus formation in the northern hemisphere (75-93% of clouds seasonally). Using a global transport model with improved dust treatment, we also explore which of Earth's deserts are the largest contributors of dust aerosol to cirrus-forming regions. We find that the meteorological environment downstream of each emission region modulates dust atmospheric lifetime and transport efficiency to the upper troposphere, so that source contributions are disproportionate to emissions. Our findings establish the critical role of dust in Earth's climate system through the formation of cirrus cloud.

Main Text:

Interactions between aerosol and clouds are a poorly understood aspect of the climate system[1]. Clouds strongly influence the balance of solar and terrestrial radiation that determines air and surface temperatures. Mineral dust aerosol particles are principal players in initiating the formation of cirrus[2–4], widespread high altitude clouds composed of ice that exert a net warming effect on the planet[5]. Natural cloud seeding by mineral dust competes with other cirrus initiation mechanisms, the dominant process then defining cirrus cloud coverage, vertical extent, microphysical properties, and brightness. Mineral dust's potential to dictate cirrus properties designate it a fundamentally important aerosol type for atmospheric radiative balance and global climate[6].

Approximately 1000-4000 Tg of dust aerosol is emitted annually from the world's arid regions[7–9], making it among the most abundant aerosol types in the atmosphere. Thick plumes visible from space account for the overwhelming bulk of atmospheric dust aerosol. These low altitude plumes (typically <6 km[10,11]) reside at temperatures too warm for cirrus formation. A tiny fraction of emitted dust particles are vertically transported to the cold upper troposphere (UT). Even with very low relative abundance (~1 in 10^3-10^5 aerosol particles), dust and other ice-nucleating particles (INP) may still effectively control cirrus cloud formation[12].

Cirrus are formed by nucleation of water into ice, a fleeting process that occurs at high altitudes and is notoriously difficult to observe directly in the atmosphere[4]. Theoretical treatments of cirrus formation are also challenging because global models must approximate the small-scale (sub-grid) variability of aerosol and ambient conditions to which nucleation is extremely sensitive[11,13].

Our ability to assess the impact of dust on the climate system and predict the effects of future changes to dust emissions is hampered by a nearly universal lack of dust aerosol abundance measurements in the cirrus-forming regions of the atmosphere. No large-scale dust concentration measurements have been reported in the background UT. Widespread geographic coverage of dust and other aerosol species can be achieved by some satellite sensors, though they lack the sensitivity to detect dust once thick plumes dissipate[14–16], only a few are altitude-resolved, and absolute concentrations are generally not reported.

In our previous studies sampling cirrus clouds directly, we confirmed that mineral dust particles were principally responsible for a limited set of northern hemispheric cirrus clouds[2]. Here we present wide-ranging measurements of dust aerosol in the background atmosphere and investigate dust sources using global models. We assess dust's influence on cirrus by combining highly sensitive measurements of dust aerosol, previous laboratory studies of dust INP activity, global simulations of air transport, and offline microphysical simulations of ice nucleation.

Mineral dust is lofted into the global upper troposphere

Mineral dust was sampled on a global scale during the NASA Atmospheric Tomography (ATom) airborne campaigns (Fig. 1). Continuous vertical profiling during north-south transects of the Pacific and Atlantic Ocean basins generated two-dimensional aerosol curtains. The Particle Analysis by Laser Mass Spectrometry (PALMS) instrument identified individual mineral dust particles and other aerosol types from their chemical fingerprints. Dust mass and number concentrations are derived by combining PALMS chemical information with size-resolved aerosol number concentration measured concurrently[17]. Over a few minutes sample time, this new, highly sensitive *in situ* measurement technique can detect dust aerosol at the minute concentrations necessary to investigate its role in cirrus formation (Fig. S1).

In Fig. 2 and S2-S4 we present the airborne measurements as global-scale maps of mineral dust in the background troposphere. Dust mass concentrations span several orders of magnitude. Most atmospheric dust is emitted as intense plumes from a few arid regions of the world (Fig. 1). As plumes dissipate into the background atmosphere, dust aerosol is transported globally and removed from the atmosphere by precipitation and surface deposition. Dust must be lofted to reach the UT where cirrus form, with convective clouds providing a direct route. However, during vertical transport dust and other aerosol are also efficiently scavenged by clouds and precipitation. From 2 to 12 km altitude, average dust mass concentrations decrease by factors of 10-1000 due to dilution and removal by clouds (Fig. 2c-e). Vertical concentration gradients vary across latitudes and are strongest over emission sources such as the tropical and northern Atlantic basin. Polar profiles have shallower or even inverted altitude gradients due to weak convection, less precipitation, and low surface emissions[18].

Global models parameterize the detailed cloud processes and aerosol losses during convective transport. Uncertainties in these processes have led to highly variable UT aerosol predictions[11], with surface-emitted aerosol often vastly over-estimated[13]. Surface-based and total column techniques to evaluate modeled aerosol do not constrain UT dust concentrations because the overwhelming majority of dust aerosol mass exists in the lower troposphere, below cirrus altitudes. In Fig. 2 CESM/CARMA[19] and GEOS/GOCART[20] dust simulations give context to the dust encountered by the aircraft. Both models use revised aerosol convective transport schemes (see Methods)[21,22] that improve the accuracy of UT dust mass concentrations x10-100 (Fig. S5). Importantly, the global simulations of mineral dust abundance are now constrained by wide-ranging *in situ* measurements that can resolve the minute quantities of dust present in the background upper troposphere.

Certain deserts are more efficient at supplying dust to the UT

Dust emission rates and atmospheric concentrations from the world's most productive source regions have been investigated in many previous airborne and ground-based measurement campaigns, frequently targeting Northern Africa[6,23–27]. Using the CESM/CARMA global model with an improved convective transport scheme, we explore how Earth's seven foremost dust emission zones (Fig. 1 black boxes) supply dust aerosol to the UT. We focus on cirrus-forming regions where supersaturated water vapor can nucleate ice onto dry particles, typically termed "deposition" nucleation (T<235 K, Fig. S6)[4].

Transport of dust to cirrus-forming regions depends on the amount of dust emitted as well as the downwind meteorological environment. North African dust emissions, primarily from the Saharan Desert, account for 60% of all emissions and dwarf other sources (Fig. 3, Table 1). Infrequent deep convection over the Sahara limits direct dust transport into the UT (Fig. S7). Once the main dust plume departs the African continent it slowly subsides and continues to experience minimal convection as it crosses the Atlantic through the Azores High. Most of the plume eventually subsides into the marine boundary layer[10], a high-loss environment where aerosol is scavenged by rain and turbulent mixing to the ocean's surface. In contrast, central Asian deserts emit only about 13% of global dust mass, yet through most of the year their contributions to UT dust are larger than North Africa (Fig. 3). After dust is lofted to several km altitude by frontal systems, further vertical transport into the UT is driven by a variety of mechanisms[28,29] such as dry convection, synoptic scale ascent, orographic uplift, and interactions with the Tibetan Plateau and the Asian Summer Monsoon[30,31]. Asian dust in the UT is then transported across the Pacific via the sub-tropical jet (Fig. S7)[28,30].

Figure 3 summarizes seasonal patterns of UT dust contributions from the seven emission zones. Surprisingly, North Africa does not overwhelm other dust sources. Asian emissions compete annually with North Africa, contributing 59-73% of dust to the northern hemisphere (NH) UT during boreal summer, despite Saharan emissions at their annual maximum. Middle Eastern desert inputs are smaller but more consistent seasonally. North America is a minor contributor, both globally and to the NH. Australia, South Africa, and South America deserts are the southern hemisphere's (SH) major sources and contribute 92.3% of the UT dust but account for only 4.3% of global UT dust by mass. All contribute similarly to the UT in the SH and have similar seasonal cycles. Tropical UT dust sources are the most varied, with SH emissions dominating during austral summer and NH taking over during other seasons. Source contributions to UT dust have a strong seasonal variability that is not commensurate with emission cycles (lines, Fig. 3), highlighting how downwind environments help modulate vertical transport.

The Fig. 3 pie charts summarize how UT dust contributions from each zone do not always scale with their annual emissions. Asia's contributions are disproportionally high and North Africa's are low so that each accounts for about 40% of global UT dust. We compare the relative efficiency of dust transport into cirrus-forming regions by normalizing UT concentrations to annual emissions for each zone in Table 1. Relative to North Africa, all other NH zones have higher vertical transport efficiencies, with Asian dust emissions being the most efficient. On a per-emissions basis, about 10 times as much Asian dust reaches cirrus-forming regions compared to North African dust. This amplified Asian transport efficiency relative to North Africa is larger than the estimated model biases for those regions (see Supplemental material) and is consistent with a recent trajectory analysis [28]. In contrast the three SH dust emission zones show less variability, with South America seeding the UT most efficiently. In both hemispheres the largest source is the least efficient at transporting dust to cirrus-forming regions. The well-known north-south emissions gradient in dust (NH/SH = 7.5) [7] is amplified in

UT concentrations (NH/SH = 22), giving the NH a considerably higher potential to induce cirrus formation by mineral dust aerosol.

Projections of future dust emission changes are highly uncertain, and even the sign is unknown[1,32]. The underlying meteorological drivers for dust emission are different across emissions zones, as are their regional responses to climate change forcings[33]. In particular, Asian emissions increasing relative to Africa[34] would further amplify the disproportionally high influence of Asian dust on cirrus.

Assessing dust's role in global cirrus cloud formation

We now evaluate the ability of dust ice-nucleating particles (INP) to generate cirrus. Climate models are unable to explicitly simulate cirrus ice nucleation because model grid cells are typically much larger (10's of km) than individual clouds, and long time steps (~1 hr) do not directly capture the transient water vapor, temperature, and INP fluctuations that lead to cloud formation. Instead, most models rely on sub-grid parameterizations of these highly sensitive variables[35,36]. In the real atmosphere, temperature and water vapor can have gradients across meter-length scales, and cloud formation occurs over seconds to minutes.

We employ a detailed microphysical model of cirrus ice nucleation at high time resolution, initialized by ATom dust and water vapor measurements (Fig. 4). Starting at the aircraft position, future air temperatures are predicted from 10-day forward trajectories calculated from the NOAA Global Forecast Systems model. High-frequency perturbations are superimposed on trajectory temperatures to simulate UT gravity waves not resolved by the model (Fig. S8), thereby providing a realistic ensemble of future temperatures that aircraft-sampled air parcels will experience. The detailed freezing model is run every hour along each future trajectory. These simulations probe the role of dust aerosol in forming *in situ* cirrus, i.e., clouds that are not directly associated with convective storms yet account for a large fraction of UT cirrus[37]. Cirrus simulations do not include freezing during convective transport, where dust aerosol is also likely to nucleate ice.

The cirrus simulations incorporate the new dust measurements (Fig. S1), which provide a critical constraint and thereby enable a realistic assessment of cirrus formation in the background atmosphere. Dust particles induce ice formation by deposition heterogeneous nucleation[4], and background aerosol freeze homogeneously as aqueous solution droplets[12]. The competition between these processes depends on dust abundance, size, and the cooling rate that drives supersaturation of water vapor with respect to ice (S_{ice}). In cases of rapid cooling or in dust-poor environments, dust aerosol has little influence on cirrus cloud properties. Not all dust particles are efficient INP[4], and the active fraction is extremely sensitive to particle size and S_{ice} (Fig. S9, S10). We employ a recent parameterization of desert dust ice nucleation efficiency based on dozens of controlled cloud formation experiments[38].

Within the 10-day simulation period, air parcels from 2759 trajectories experienced cirrus formation events at some point. Heterogeneous nucleation on mineral dust aerosol was solely responsible for 71% of cirrus clouds, and the rest were formed by homogeneous freezing (Fig. 5). The relative contribution of dust to ice nucleation is fairly constant above 195 K (Fig. 5a). The two competing nucleation mechanisms act to distribute the available water vapor into drastically different ice crystals populations (Fig. 5b). Homogeneous freezing of the relatively abundant aqueous aerosols distributes the condensable water vapor into numerous small ice crystals and generates cirrus with high solar reflectivity. Conversely, most dust-induced cirrus initially contain fewer (and given the same water vapor, larger) ice crystals and are optically thinner[37], thereby exerting a smaller radiative effect. If we consider only the most radiatively relevant cirrus having abundant ice crystals (N_i>10 L^{-1}), dust still initiates about half (47%) of cirrus globally and 72% in the NH extra-tropics.

Simulations that artificially suppressed nucleation on dust reveal that dust aerosol changes cloud properties in two important ways (Fig. 5b). First, dust increases cirrus occurrence by 42% (from 1945 to 2759 cases). Second, dust inhibits the formation of homogeneously nucleated, more reflective clouds in 59% of the homogeneous cases (1153 out of 1945). Global modeling studies suggest that cloud radiative effects and climate sensitivity depend strongly on ice sedimentation rates that scale with crystal size[39,40]. If dust nucleation were not considered when simulating cirrus formation, reduced sedimentation rates will alter estimates of cloud radiative effects, UT temperatures, and surface temperature responses to greenhouse gas emissions.

Air parcel trajectories span much of the global upper troposphere (Fig. S11). Dust dominates cirrus formation in the northern extra-tropics (seasonally 75-93% of cirrus cases, Fig. 5c). Dust-induced cirrus occurs throughout the year in the NH (Fig. S12), with the highest observed dust concentrations in springtime leading to an increasingly dominant effect on cirrus. Despite generally lower dust abundance in the SH extra-tropics, dust impact on cirrus formation is still significant (58-71% of cirrus cases). Tropical and subtropical air parcels experienced fewer freezing events, and despite strong dust emissions within those latitudes, very low UT concentrations reduced dust's influence on cirrus (34-63%). The tropical tropopause layer (TTL) above 13 km altitude is minimally sampled by air trajectories (Fig. S11), and therefore dust's influence on TTL cirrus cannot be fully resolved by this analysis.

The analysis confirms that dust aerosol concentration is the principal limiting factor to the cirrus formation mechanism across all seasons and measurement regions (Fig S13). Seasonal differences in temperature, RH, and atmospheric vertical motion add variability to the dust-induced cirrus fraction. Heterogeneous nucleation becomes the dominant cirrus-forming mechanism in regions where median dust concentrations are above ~10 L^{-1}, and at 100 L^{-1} nearly all *in situ* cirrus are formed by dust aerosol only. The cirrus studied here appear more sensitive to dust aerosol than higher altitude TTL cirrus[41], which required greater dust concentrations to be similarly affected.

Observational studies support the cirrus simulation results. Simulated occurrence frequencies of non-convective cirrus qualitatively match the latitude dependence of cirrus detected by satellite[42], with sub-TTL cirrus maxima between 40 and 70°. Satellite and direct sampling studies infer the competition between homogeneous and heterogeneous nucleation mechanisms from cirrus properties. In broad sampling studies at similar altitudes to ATom, high ice crystal concentrations (N_i >500 L^{-1}) indicative of young clouds formed by homogeneous freezing were rarely observed[41,43], <1% and <10%. A large fraction (40-90%) of cirrus below the TTL were very thin (N_i<15 L^{-1}), consistent with Fig. 5. In another extensive study, a high fraction of non-convective cirrus were consistent with heterogeneous nucleation or a combination of both mechanisms[37]. Some observations indicate higher levels or broader regions of clear-sky S_{ice} in the SH[44,45], consistent with homogeneous freezing being more common than in the NH. Similarly, satellite sensors observe higher N_i in mid and high latitudes during winter when regional dust emissions are lower[46,47]. However, other analyses of water vapor or cirrus particle concentrations suggest that systematic differences in NH-SH S_{ice} are still unclear[48,49].

This study demonstrates that mineral dust aerosols convectively lofted to the UT are abundant enough to initiate cirrus cloud formation during all seasons throughout the extra-tropics, including the SH. Our approach applied to the ATom cases provides the most quantitative analysis to date of dust's influence on cirrus formation in remote regions. Non-dust INP candidates are less well constrained in their UT abundance and nucleation efficiency. Although we consider dust to be the most important (abundant and active) INP type in the UT, other particle types may contribute seasonally or regionally. Furthermore, we do not consider heterogeneous nucleation mechanisms that occur at warmer temperatures, such as immersion freezing, where dust is also effective. In this way the analysis here defines a lower limit to the influence of dust heterogeneous nucleation on the occurrence and properties of global cirrus.

Acknowledgments:

The authors thank Maximilian Dollner and Bernadett Weinzierl for cloud particle measurements to exclude cloudy flight segments, Matthews Richardson, Frank Erdesz, and David Thomson for technical support, and Daniel Cziczo for valuable input. The ATom mission was supported by NASA's Earth System Science Pathfinder Program EVS-2 funding. Participation in the ATom mission by KDF, GPS, CJW, CAB, DMM, and ER was supported by NOAA climate funding and NASA award NNH15AB12I. PY was supported by the second Tibetan Plateau Scientific Expedition and Research Program (STEP, 2019QZKK0604). The CESM project is supported partly by the National Science Foundation. AK was supported by the Austrian Science Fund's Erwin Schrodinger Fellowship J-3613. GEOS development in the Global Modeling and Assimilation Office is funded by NASA's Modeling, Analysis and Prediction (MAP) program. Resources supporting GEOS were provided by the NASA High-End Computing (HEC) Program through the NASA Center for Climate Simulation (NCCS) at Goddard Space Flight Center. HB was supported by NASA award NNX17AG31G. PRC was supported by the MAP-funded Chemistry-Climate Modeling (CCM) project (600-17-6985).

Author contributions:

KDF wrote the paper with contributions from all authors. KDF, GPS, CAB, AK, CJW, DMM, GSD, and TB collected airborne data. PY and KHR provided CESM-CARMA model results. HB, ASD, and PRC provided GEOS model results. ER provided forward trajectory results. EJJ provided cirrus model results.

Competing interests:

The authors declare no competing interests.

Tables:**Table 1.** Annual dust surface emissions and average UT concentrations sourced from each emission zone[a].

	--------- Surface emissions ---------			--------- UT concentrations ---------		
Dust Emission Zone	Total emissions (Tg yr^{-1})	% of total	Relative to largest hemispheric source†	Average UT conc. (ng m^{-3})	% of total	Relative to largest hemispheric source and relative to emissions‡
Northern hemisphere sources						
1. North Africa	1338	59.8%	≡ 1	2.06	39.8%	≡ 1
2. Asia	298	13.3%	0.22 (0.17 – 0.29)	2.03	39.1%	9.7 (1.8 – 18.3)
3. Middle East	280	12.5%	0.21 (0.15 – 0.34)	0.76	14.7%	2.8 (0.9 – 6.6)
4. North America	71	2.5%	0.04 (0.03 – 0.05)	0.11	2.1%	2.6 (0.3 – 7.6)
Southern hemisphere sources						
5. Australia	107	4.8%	≡ 1	0.09	1.8%	≡ 1
6. South Africa	85	3.8%	0.80 (0.67 – 0.98)	0.06	1.1%	1.5 (0.5 – 4.4)
7. South America	71	3.2%	0.66 (0.45 – 0.87)	0.07	1.4%	3.4 (0.9 – 16.2)

[a] Data are from 2014-2018 simulations using the revised CESM/CARMA model.

†Annual average of monthly ratios (monthly ranges in parentheses)

‡The relative effectiveness of emissions from each zone contributing to UT dust, calculated for each month as (UT conc. from zone / UT conc. from largest source) / (emissions from zone / emissions from largest source), then averaged (monthly range in parentheses). Values are normalized to the largest hemispheric emission source.

Figure Legends:

Fig. 1. Global-scale airborne sampling of mineral dust aerosol during four NASA ATom campaigns. Flight tracks are colored by seasonal deployment and shaded by altitude from 0.2 to 13 km (light to dark). Continents are colored by satellite-derived land type (https://modis.gsfc.nasa.gov/data/dataprod/mod12.php), where brown denotes arid regions that are the predominant sources of mineral dust to the atmosphere. Black boxes encompass seven principal dust emission zones.

Fig. 2. Dust aerosol measurements and simulations during ATom1 in Aug, 2016. Airborne *in situ* measurements over the Pacific basin (a,c), Atlantic basin (b,d), and polar regions for all longitudes (e) are compared to two models. Flight tracks (top panels) are colored by measured dust mass concentration on a log scale. Background shading shows simulated CESM/CARMA dust concentrations, plotted as vertical curtains at the aircraft location. Lines delineate five

latitude bands (polar/mid-latitudes/tropics, see Methods). In the lower panels, measured dust concentrations (solid) are compared to the CESM/CARMA (long dash) and GEOS/GOCART (short dash) simulations for each latitude band. See Fig. S2-S4 for other seasons and variability. Several of the planet's largest dust features were captured, including the intense North African plume observed over the mid-Atlantic a few days after emission (b) and again >10 days downwind over the Pacific Ocean at similar altitudes (a). See Supplementary Information for discussion of spatial and seasonal patterns.

Fig. 3. Annual cycle of UT dust sourced from each desert emission zone from the revised CESM/CARMA model. (a-g) Shading indicates each source's fractional contribution to UT dust mass as a function of latitude (left axis) and season. Annual averages are listed as percent. Lines (right axis) compare fractional UT concentrations (black) and surface emissions (orange) within the northern (solid) and southern (dash) hemispheres. Pie charts (h) are global annual averages of surface emissions and UT dust contributions from each emission zone.

Fig. 4. Predicting cirrus formation by combining *in situ* measurements with cloud-aerosol simulations. (1) Dust aerosol, water vapor, and temperature are measured from aircraft during continuous vertical profiling, creating a global-scale map of initial conditions. (2) The future movement of each sampled air parcel is calculated from meteorological wind fields. Air parcels that ascend are cooled, whereby cirrus formation becomes possible. (3) Detailed microphysical simulations of cirrus formation are performed along each air parcel's future trajectory to investigate the competition between dust heterogeneous nucleation and homogeneous freezing of background aqueous aerosol (see Methods). Illustration courtesy of K. Bogan, CIRES, University of Colorado Boulder.

Fig. 5. Mineral dust's role in global cirrus cloud formation evaluated from all ATom deployments. a) Heterogeneous nucleation on mineral dust (brown curves) dominates the freezing mode. Homogeneous freezing on aqueous aerosol (green) can occur where dust concentrations are very low or where rapid cooling produces highly super-saturated conditions quickly. Solid lines denote all cirrus freezing events, and dotted lines are for cirrus with ice concentrations N_i>10 L^{-1} (see text). b) Dust-induced freezing generates more frequent clouds with lower ice crystal concentrations. If dust heterogeneous nucleation is suppressed (blue) cirrus clouds with higher ice concentrations form instead. c) The latitudes for cirrus freezing events are compiled for all ATom cases (left axes). Seasonal distributions are shown in Fig. S12. Gray shading shows the sample space (number of 1-hr data points) for all air parcel trajectories. Measured dust concentrations (right axis) are averaged for the five latitude ranges in Fig. 2.

References:

1. Boucher, O. *et al.* Clouds and Aerosols. in *Climate Change 2013: The Physical Science Basis. Contribution of Working Group I to the Fifth Assessment Report of the Intergovernmental Panel on Climate Change*, 571-740 (eds. Stocker, T.F., D. Qin, G.-K. Plattner, M. Tignor, S.K. Allen, J. B. & A. Nauels, Y. Xia, V. B. and P. M. M.) (Cambridge University Press, Cambridge, United Kingdom and New York, NY, USA, 2013).
2. Cziczo, D. J. *et al.* Clarifying the dominant sources and mechanisms of cirrus cloud

formation. *Science* **340**, 1320–4 (2013).

3. Twohy, C. H. Measurements of Saharan dust in convective clouds over the tropical eastern Atlantic Ocean. *J. Atmos. Sci.* **72**, 75–81 (2015).
4. Kanji, Z. A. *et al.* Overview of Ice Nucleating Particles. *Meteorol. Monogr.* **58**, 1.1-1.33 (2017).
5. Lohmann, U. & Gasparini, B. A cirrus cloud climate dial? *Science* **357**, 248–249 (2017).
6. Knippertz, P., Stuut, J.-B. W. & Eds. *Mineral Dust*, 267-326 (Springer, Dordrecht, Netherlands, 2014). doi:10.1007/978-94-017-8978-3.
7. Huneeus, N. *et al.* Global dust model intercomparison in AeroCom phase I. *Atmos. Chem. Phys.* **11**, 7781–7816 (2011).
8. Kok, J. F. *et al.* Smaller desert dust cooling effect estimated from analysis of dust size and abundance. *Nat. Geosci.* **10**, 274–278 (2017).
9. Cakmur, R. V. *et al.* Constraining the magnitude of the global dust cycle by minimizing the difference between a model and observations. *J. Geophys. Res. Atmos.* **111**, 1–24 (2006).
10. Yu, H. *et al.* Quantification of trans-Atlantic dust transport from seven-year (2007-2013) record of CALIPSO lidar measurements. *Remote Sens. Environ.* **159**, 232–249 (2015).
11. Koffi, B. *et al.* Evaluation of the aerosol vertical distribution in global aerosol models through comparison against CALIOP measurements: AeroCom phase II results. *J. Geophys. Res. Atmos.* **121**, 7254–7283 (2016).
12. Pruppacher, H. R. & Klett, J. D. *Microphysics of Clouds and Precipitation*. vol. **18**, 287-355 (Springer, Dordrecht, Netherlands, 2010).
13. Kipling, Z. *et al.* Constraints on aerosol processes in climate models from vertically-resolved aircraft observations of black carbon. *Atmos. Chem. Phys.* **13**, 5969–5986 (2013).
14. Sayer, A. M. *et al.* Satellite Ocean Aerosol Retrieval (SOAR) algorithm extension to S-NPP VIIRS as part of the “Deep Blue” aerosol project. *J. Geophys. Res. Atmos.* **123**, 380–400 (2018).
15. Shi, Y. *et al.* A critical examination of spatial biases between MODIS and MISR aerosol products-application for potential AERONET deployment. *Atmos. Meas. Tech.* **4**, 2823–2836 (2011).
16. Winker, D. M. *et al.* The global 3-D distribution of tropospheric aerosols as characterized by CALIOP. *Atmos. Chem. Phys.* **13**, 3345–3361 (2013).
17. Froyd, K. D. *et al.* A new method to quantify mineral dust and other aerosol species from aircraft platforms using single-particle mass spectrometry. *Atmos. Meas. Tech.* **12**, 6209–6239 (2019).
18. Bullard, J. E. *et al.* High-latitude dust in the Earth system. *Rev. Geophys.* **54**, 447–485 (2016).
19. Yu, P. *et al.* Evaluations of tropospheric aerosol properties simulated by the Community Earth System Model with a sectional aerosol microphysics scheme. *J. Adv. Model. Earth Syst.* **7**, 865–914 (2015).
20. Colarco, P., da Silva, A., Chin, M. & Diehl, T. Online simulations of global aerosol distributions in the NASA GEOS-4 model and comparisons to satellite and ground-based aerosol optical depth. *J. Geophys. Res.* **115**, D14207 (2010).
21. Yu, P. *et al.* Efficient In-Cloud Removal of Aerosols by Deep Convection. *Geophys. Res. Lett.* **46**, 1061–1069 (2019).
22. Schill, G. P. *et al.* Widespread biomass burning smoke throughout the remote troposphere.

Nat. Geosci. **13**, 422–427 (2020).

23. Formenti, P. *et al.* Regional variability of the composition of mineral dust from western Africa: Results from the AMMA SOP0/DABEX and DODO field campaigns. *J. Geophys. Res. Atmos.* **113**, 1–12 (2008).
24. Lieke, K. *et al.* Particle chemical properties in the vertical column based on aircraft observations in the vicinity of Cape Verde Islands. *Tellus, Ser. B Chem. Phys. Meteorol.* **63**, 497–511 (2011).
25. Weinzierl, B. *et al.* The Saharan aerosol long-range transport and aerosol-cloud-interaction experiment: Overview and selected highlights. *Bull. Am. Meteorol. Soc.* **98**, 1427–1451 (2017).
26. Ryder, C. L. *et al.* Coarse-mode mineral dust size distributions, composition and optical properties from AER-D aircraft measurements over the tropical eastern Atlantic. *Atmos. Chem. Phys.* **18**, 17225–17257 (2018).
27. Price, H. C. *et al.* Atmospheric ice-nucleating particles in the dusty tropical Atlantic. *J. Geophys. Res. Atmos.* **123**, 2175–2193 (2018).
28. Wiacek, A., Peter, T. & Lohmann, U. The potential influence of Asian and African mineral dust on ice, mixed-phase and liquid water clouds. *Atmos. Chem. Phys.* **10**, 8649–8667 (2010).
29. Tsai, F., Chen, G. T.-J., Liu, T.-H., Lin, W.-D. & Tu, J.-Y. Characterizing the transport pathways of Asian dust. *J. Geophys. Res.* **113**, D17311 (2008).
30. Xu, C., Ma, Y., Yang, K. & You, C. Tibetan Plateau impacts on global dust transport in the upper troposphere. *J. Clim.* **31**, 4745–4756 (2018).
31. Ma, J. *et al.* Modeling the aerosol chemical composition of the tropopause over the Tibetan Plateau during the Asian summer monsoon. *Atmos. Chem. Phys.* **19**, 11587–11612 (2019).
32. Mahowald, N. M. Anthropocene changes in desert area: Sensitivity to climate model predictions. *Geophys. Res. Lett.* **34**, 1–5 (2007).
33. Kok, J. F., Ward, D. S., Mahowald, N. M. & Evan, A. T. Global and regional importance of the direct dust-climate feedback. *Nat. Commun.* **9**, (2018).
34. Chin, M. *et al.* Multi-decadal aerosol variations from 1980 to 2009: A perspective from observations and a global model. *Atmos. Chem. Phys.* **14**, 3657–3690 (2014).
35. Gettelman, A. *et al.* Global simulations of ice nucleation and ice supersaturation with an improved cloud scheme in the Community Atmosphere Model. *J. Geophys. Res.* **115**, D18216 (2010).
36. Kuebbeler, M., Lohmann, U., Hendricks, J. & Kärcher, B. Dust ice nuclei effects on cirrus clouds. *Atmos. Chem. Phys.* **14**, 3027–3046 (2014).
37. Krämer, M. *et al.* A microphysics guide to cirrus – Part 2: Climatologies of clouds and humidity from observations. *Atmos. Chem. Phys.* **20**, 12569–12608 (2020).
38. Ullrich, R. *et al.* A new ice nucleation acive site parameterization for desert dust and soot. *J. Atmos. Sci.* **74**, 699–717 (2017).
39. Mitchell, D. L., Rasch, P., Ivanova, D., McFarquhar, G. & Nousiainen, T. Impact of small ice crystal assumptions on ice sedimentation rates in cirrus clouds and GCM simulations. *Geophys. Res. Lett.* **35**, L09806 (2008).
40. Sanderson, B. M., Piani, C., Ingram, W. J., Stone, D. A. & Allen, M. R. Towards constraining climate sensitivity by linear analysis of feedback patterns in thousands of perturbed-physics GCM simulations. *Clim. Dyn.* **30**, 175–190 (2008).

41. Jensen, E. J. *et al.* Heterogeneous ice nucleation in the tropical tropopause layer. *J. Geophys. Res. Atmos.* **123**, 12,210-12,227 (2018).
42. Mace, G. G. *et al.* A description of hydrometeor layer occurrence statistics derived from the first year of merged Cloudsat and CALIPSO data. *J. Geophys. Res. Atmos.* **114**, 1–17 (2009).
43. Petzold, A. *et al.* Upper tropospheric water vapour and its interaction with cirrus clouds as seen from IAGOS long-term routine: In situ observations. *Faraday Discuss.* **200**, 229–249 (2017).
44. Haag, W. *et al.* Freezing thresholds and cirrus cloud formation mechanisms inferred from in situ measurements of relative humidity. *Atmos. Chem. Phys.* **3**, 1791–1806 (2003).
45. Gettelman, A., Fetzer, E. J., Eldering, A. & Irion, F. W. The global distribution of supersaturation in the upper troposphere from the Atmospheric Infrared Sounder. *J. Clim.* **19**, 6089–6103 (2006).
46. Mitchell, D. L., Garnier, A., Pelon, J. & Erfani, E. CALIPSO (IIR–CALIOP) retrievals of cirrus cloud ice-particle concentrations. *Atmos. Chem. Phys.* **18**, 17325–17354 (2018).
47. Sourdeval, O. *et al.* Ice crystal number concentration estimates from lidar-radar satellite remote sensing - Part 1: Method and evaluation. *Atmos. Chem. Phys.* **18**, 14327–14350 (2018).
48. Kahn, B. H., Gettelman, A., Fetzer, E. J., Eldering, A. & Liang, C. K. Cloudy and clear-sky relative humidity in the upper troposphere observed by the A-train. *J. Geophys. Res. Atmos.* **114**, 1–16 (2009).
49. Diao, M., Zondlo, M. A., Heymsfield, A. J. & Beaton, S. P. Hemispheric comparison of cirrus cloud evolution using in situ measurements in HIAPER Pole-to-Pole Observations. *Geophys. Res. Lett.* **41**, 4090–4099 (2014).

Methods:

The NASA Atmospheric Tomography Mission (ATom) airborne sampling campaigns

During the NASA ATom mission between 2016 and 2018, the NASA DC8 flying research laboratory executed four global-scale sampling campaigns over the Pacific and Atlantic Ocean basins[50]. ATom was designed to evaluate satellite measurements and global models of gas-phase and aerosol species. The vast majority of sampling time occurred in the remote atmosphere, 100’s to 1000’s of km from continental emission sources. Flights spanned latitudes from about 86 °S to 82 °N. The aircraft executed constant vertical profiles from 0.2 to 13 km altitude, with 5-15 minute legs of constant altitude at the top and bottom of each profile. Despite its broad spatial coverage and multiple deployments, the ATom data set does not constitute a climatology. An analysis of the representativeness of ATom sampling is pending[51]. We analyze measurements from all four aircraft deployments, ATom1 (Jul 29 – Aug 23, 2016), ATom2 (Jan 26 – Feb 21, 2017), ATom3 (Sept 28 – Oct 27, 2017), and ATom4 (Apr 24 – May 21, 2018). We exclude low altitude flight segments near airports and the Aug 23, 2016 transit flight over the continental US. In Fig. 2 and elsewhere we average dust concentrations across broad latitude bands, defined as polar (>60°), mid-latitudes (27°-60°), or tropical/subtropical (<27°) for all deployments. Longitude 71°W separates Pacific and Atlantic Ocean basins. ATom aircraft data for each flight are publically available at https://daac.ornl.gov/ATOM/guides/ATom_merge.html.

Aerosol concentration measurements

Size-resolved aerosol concentration from 0.003–4.8 μm[52] was measured by combining two nucleation-mode aerosol size spectrometers (NMASS)[53], a Droplet Measurement Technologies Ultra High Sensitivity Aerosol Spectrometer (UHSAS)[54], and a TSI, Incorporated Laser Aerosol Spectrometer (LAS). The UHSAS and LAS optical spectrometers encompass the mineral dust size range reported here, D>0.1–4.8 μm. Particle diameters were derived from optical spectrometer calibrations using ammonium sulfate, which has a refractive index that is also appropriate for many mineral dusts and most other tropospheric particle types[17,52,54]. Sample flows were 0.06 and 0.1 lpm, respectively.

Air was isokinetically sampled using a forward-facing, shrouded, diffuser inlet designed by the University of Hawaii. This inlet transmits aerosol with approximately 100% efficiency for sizes up to ~4 μm aerodynamic diameter at low altitude, whereby efficiency drops to 50% at sizes greater or equal to 5.0 μm (~3 and ≥3.2 μm at 12 km)[55]. In characterizing the aircraft inlet, the authors reported the 50% cutpoint sizes as lower diameter limits due to limited large particle statistics in their reference measurement, and they acknowledged that actual efficiencies could be higher[55]. A reliable transmission efficiency curve cannot be generated. Therefore, while it is likely that some undersampling occurred at the large end of the reported size range (D>3-4 μm), due to the ambiguity in the aircraft inlet inefficiency no attempt was made to adjust measured dust concentrations[52]. Supermicron particle number concentrations were scaled to account for sub-isokinetic sampling and losses in instrument tubing, with typical scaling factors of x0.97-1.04 for 1 μm particles and x3.0-3.4 for 4 μm particles[52]. Cloudy flight segments are excluded at 1 sec resolution based on data from a wing-mounted cloud particle probe.

Mineral dust aerosol measurements using PALMS

The NOAA Particle Analysis by Laser Mass Spectrometry (PALMS) airborne single-particle mass spectrometer instrument has been described in detail previously[56,57]. PALMS characterizes the size and chemical composition of individual aerosol particles from about 0.1–5 μm in diameter. Single-particle mass spectra are post-processed to classify each particle into a compositional type and that are then counted to determine their relative abundance[17,58].

Mineral dust particles are identified as spectra having multiple crustal metal signatures such as silicon, aluminum, iron, and calcium, and often with trace amounts of alkalis, barium, tin, antimony, or lanthanides. The dust particle class is very diverse, with several different composition sub-types representing a wide variety of mineralogies. Typical mineral dust spectra have distinctive signatures and are easily differentiated from other particle types that also contain metals, such as biomass burning, alkali salts, meteoric, and oil combustion. Dust classification is further refined using a cluster analysis routine that groups similar spectra[58]. Manual sorting of clusters and reclassification of a minor fraction of the dust spectra further reduces misclassification error, estimated to be <5%[17].

Mineral dust quantification using PALMS and aerosol size spectrometers

PALMS and other single-particle mass spectrometer instruments do not measure aerosol concentrations directly because unlike commercial size spectrometers, particle detection efficiency is a strong and variable function of size. Recently, we developed a method to combine PALMS size-resolved composition with size-resolved absolute concentration measured over the same size range by optical particle spectrometers instruments[17]. Briefly, the fractional abundance of mineral dust within a size range measured by PALMS is multiplied by the absolute concentration within that size range measured by aerosol size spectrometers[52] to derive number, surface area, volume, and mass concentration of mineral dust aerosol from 0.1 to 4.8 μm geometric diameter. Note that the large size limit is approximate since aircraft inlet sampling efficiency becomes increasingly less certain above about ~3-4 μm aerodynamic diameter (see previous sections)[52,55]. Particle spectrometer number distributions are converted to volume assuming spherical shape, and mineral dust density is prescribed as 2.5 g cm^{-3} to convert volume to mass. Concentrations are reported at ambient temperature and pressure conditions, except standard concentrations are reported (1013 mbar, 273.15 K) are reported for Fig. 2 and S2-S4.

PALMS and the aerosol size spectrometers sampled continuously during flight. Mass concentration products are averaged every 3 minutes of sampling time. Principal uncertainties in the derived dust mass and number concentrations include the statistical sampling of aerosol and the volume concentration measurement from size spectrometers. Estimated statistical uncertainties from PALMS statistical sampling and identification of mineral dust are 50% at 0.01 $\mu g\ m^{-3}$ and 25% at 1 $\mu g\ m^{-3}$ [17]. Uncertainties in aerosol size spectrometer concentrations over 3 minutes are estimated as 7-17% for number and 30-131% in volume and principally due to atmospheric variability of sparse $D>0.5\ \mu m$ aerosol[52]. We estimate the LOD as the minimum concentration for 1 dust particle detected per sample time. For 3 min samples, typical mass LODs are ~0.0001-0.01 $\mu g\ m^{-3}$ (Fig. S1B) above 3 km altitude. Sample times for dust number concentrations were typically 6 min but up to 24 min for flight segments at constant altitude (range <1 km). Typical LODs in the UT are ~0.5-10 L^{-1} (Fig. S1A). Number concentrations are reported for the size range D=0.18 to 4.8 μm.

Cirrus-forming regions may contain mineral dust particles that are too large to sample by the aircraft inlet and *in situ* instruments. However, dust number concentrations for large sizes will be relatively low. By extrapolating the number distributions from ~4 to 25 μm diameter using a log-linear function (Fig. S10a), we estimate that large, unsampled dust particles contribute <7% of the total dust number concentration for all ATom cases, yielding a negligible change (<1%) in cirrus initiation statistics.

Airborne measurements of gases and temperature

Water vapor was measured by the Diode Laser Hygrometer (DLH), an external-path diode laser absorption instrument which has flown on the DC-8 and numerous other airborne platforms[59,60]. DLH water vapor measurements have been intercompared and validated under conditions relevant to this study[61]. The temporal resolution of these measurements is greater than 20 Hz; the spatial resolution is approximately 10 m in the horizontal and 1 m in the vertical.

The Meteorological Measurement System[62] measures ambient dynamic temperature from open wire platinum sensor. Accurate and science quality static temperature is indirectly derived from 3D wind aero-dynamic calibration using aircraft induced maneuvers.

Global simulations of mineral dust aerosol using CESM/CARMA

We use the NSF/NCAR Community Earth System Model (CESM) coupled with the Community Aerosol and Radiation Model for Atmospheres (CARMA) sectional aerosol model [19,21,63,64]. CARMA tracks 20 discrete size bins from 0.1 µm to 17.4 µm in diameter for internally mixed aerosols including mineral dust, sea-salt, organic material, black carbon and sulfate. Integrated dust mass concentration is calculated between 0.1 and 4.5 µm for comparison with PALMS dust mass concentrations (Fig 2, S2 through S5). The model runs at 1.9x2.5 degree resolution and 56 vertical layers from the surface to ~45 km. At every time step, CESM/CARMA is nudged to the Goddard Earth Observing System model v.5 (GEOS5) dynamic meteorological wind and temperature fields. To compare the modeled dust mass concentrations with ATom measurements (Fig. 2, S2-S5) we extract model output at the aircraft location and time.

The dust emission source function depends on particle size and surface wind speed [65–67]. Some dust sources such as co-emission with biomass burning smoke[68] and resuspension from glaciers[18,69] are not specifically included. CARMA simulates several dust removal processes at the sub-grid level. Dust can be scavenged below cloud by raindrops. Also, dust can be activated as cloud condensation nuclei, then subsequently removed both at and above the cloud base. The parameterization of deep convection in the CESM model assumes a stationary state of an ensemble of convective plumes, for which the transport of water, temperature and momentum has been widely validated[70]. Yu et al.[21] revised CESM/CARMA convective removal processes based on the methodology of previous studies[71,72]. Aerosol removal was constrained by comparing modeled vertical distributions of sea-salt and black carbon against the ATom datasets. In the present study, we found that simulations with a tuning parameter ($ract = 0.02\ \mathrm{hPa}^{-1}$) in the activation term of Yu et al. best matched ATom mineral dust mass concentration measurements. For the source apportionment runs (Fig 3, Table 1, S6, S7) we conducted 8 simulations, in each of which only a single source region emitted dust (7 boxed regions in Fig. 1, plus the global remainder that accounted for <0.1% of total emissions and UT concentrations). The simulations cover 2014 to 2018, preceded by a 3-year spin-up. Monthly and annual mean model output are used to determine the dust UT contributions. Dust emissions and atmospheric concentrations are calculated for the entire CARMA size range.

Global simulations of mineral dust aerosol using GEOS/GOCART

Dust is simulated in the Goddard Chemistry, Aerosol, Radiation, and Transport (GOCART) aerosol module[20,73,74] in the Goddard Earth Observing System model v.5 (GEOS) framework.[75]. GOCART simulates BC, organic carbon, sulfate, nitrate, ammonium, dust, and sea salt. For the ATom comparisons, GEOS/GOCART was run at a global ~50-km horizontal resolution with 72 vertical pressure layers from the surface up to 0.01 mbar (~85 km). The dynamical time step was 450 s. The model was run in 'replay mode', which resets the model dynamical state every 6 h to a balanced state provided by the Modern-era Reanalysis for Research and Applications v.2 atmospheric reanalysis. A 2.5-yr simulation was conducted from the beginning of 2016 to cover all of the ATom missions. The first half of 2016 was used as a spin-up period. For model-measurement comparisons, dust mass concentrations are extracted from the model domain at the time and location of the aircraft using a linear interpolation method in both space and time.

The emission of dust particles is calculated online based on the GEOS dynamic meteorological fields including surface wind and soil moisture using a topographic-based algorithm[65]. Simulated dust size bins are 0.2–2, 2–3.6, 3.6–6.0, 6.0–12, and 12–20 μm dry optical diameter. For comparison to PALMS dust mass concentrations (Fig 2, S2-S5), integrated mass is calculated by summing the first two bins, 0.2–3.6 μm, using densities of 2500 and 2650 kg m^{-3} for the first and second bin, respectively. Dust particles are removed by dry and wet deposition via impaction collection of rain/cloud droplets on dust particles. Table S1 describes the treatment of dust wet scavenging in GEOS for the previous baseline case (R7), a sensitivity experiment (R9), and the revised treatment (R23) that was recently formulated using ATom biomass burning aerosol data[22].

Model evaluation using ATom measurements

The reported dust mass concentrations characterize the atmosphere at the time and location of measurement. Large-scale models should extract simulated dust concentrations that are co-located with aircraft sampling. To assess the skill of CESM/CARMA and GEOS/GOCART to reproduce the PALMS mineral dust observations, we calculated the mean log bias and centered root mean squared log error (CRMSLE) of the models following the method of Schill et al.[22] (Fig. S5). A mean log bias of 1 means the model is biased by an order of magnitude ($10^1 = 10$). This analysis can emphasize disagreement at low concentrations since relative errors can be large near detection limits.CRMSLE represents the width of the errors around the mean log bias and is analogous to the standard deviations of the errors if they are normally distributed.

In some environments, PALMS observed zero dust particles for a significant fraction of data samples. Excluding these samples from the log bias analysis would artificially skew the biases to lower values. Therefore, for samples with zero dust particles, the measured mass concentration is approximated as half the LOD (see Fig. S1).

Forward trajectories of air transport

Forward trajectories were calculated using the Traj3D model[76,77] run with National Centers for Environmental Predictions (NCEP) Global Forecast System (GFS) 0.25°x0.25° resolution meteorology (https://www.ncdc.noaa.gov/data-access/model-data/model-datasets/global-forcast-system-gfs). Trajectories were initialized along the flight track each minute and run forward for 10 days with a time resolution of one hour.

Cirrus ice nucleation simulations

Our objective is to investigate the impact of mineral dust particles on cirrus formation and initial crystal concentrations. We simulate the competition between homogeneous freezing of aqueous aerosols and heterogeneous ice nucleation on dust particles using a box model. After nucleation, processes such as differential sedimentation, entrainment, and aggregation conspire to reduce ice concentrations as cirrus evolve[78–81]. Simulation of these subsequent processes is beyond the scope of the current study. See Supplementary Information for a discussion of nucleation mechanisms and contributions by non-dust INP types.

As an air parcel cools and the supersaturation over ice (S_{ice}) increases above about 1.1, heterogeneous nucleation on dust particles produces the first ice crystals. If the concentration of ice crystals nucleated on dust particles is sufficient and the cooling is slow enough, then depositional growth of these ice crystals will deplete vapor and halt the rising S_{ice} before the threshold for homogeneous freezing (S_{ice}=1.45-1.70, depending on temperature) is reached. In this case, the ice concentration will be determined by the abundance of dust heterogeneous nuclei. If the dust concentration is sufficiently low and cooling is sufficiently rapid, then S_{ice} will continue to rise after heterogeneous ice nucleation on dust has occurred, and homogeneous freezing will ultimately dominate the ice concentration. The ice concentration just after nucleation will generally be the maximum value over the lifecycle of the cirrus cloud. To represent a cloud we track the nucleation and growth of hundreds of individual ice crystals[82] and associated changes in water vapor. This Lagrangian approach avoids the numerical diffusion associated with growth/sublimation of ice crystals in an Eulerian (bin) model.

Aqueous aerosols are represented by a log-normal size distribution with a mode radius of 0.015 μm, a standard deviation of 2 and a concentration of 100 cm^{-3}. Results are not strongly sensitive to the aqueous aerosol size distribution nor their concentration. Homogeneous freezing rates are calculated using a water activity parameterization[83]. For representation of heterogeneous nucleation on dust particles, we use the ice nucleation active site (INAS) density approach[41,84] with a measurement-based parameterization of dust active site density that depends on ice saturation ratio and temperature [38]. A fundamental assumption is that the ice nucleation activity of UT dust is accurately represented by the laboratory experiments on desert dust samples. Dust particles can accumulate coatings of soluble material during atmospheric aging, and some laboratory studies indicate that thick coatings reduce nucleation efficiency[85,86]. However, preliminary analysis with PALMS indicates that for these and similar laboratory experiments, dust samples were subjected to coatings that are likely much thicker (and possibly more deactivating) than experienced by typical atmospheric dust particles. Mineral dust size distributions are taken from the ATom measurements (see Fig. S10). Dust particles are depleted from the size distribution as heterogeneous nucleation takes place.

Cooling rate is a critical factor controlling the competition between heterogeneous and homogeneous nucleation and the concentration of ice crystals[87,88]. We use a parameterized wave spectrum[82] to superimpose high-frequency temperature perturbations to simulate gravity waves that typically define UT cooling rates. The wave amplitudes were adjusted based on recent analyses of superpressure balloon measurements[89,90].

The parcel-model ice nucleation simulations are initiated for all aircraft sample points with $T \leq 235$ K and where $S_{ice} > 0.9$ at any point along the 10-day forward trajectory, yielding 2759 separate cases from 23590 total calculated trajectories. Mixing of air parcels is not considered in this analysis. If more than 90% of the dust particles are depleted by ice nucleation, and the S_{ice} has decreased to less than 1.03, we assume no further nucleation will take place. As S_{ice} rises with decreasing temperature, dust heterogeneous nucleation always precedes homogeneous freezing, resulting in many clouds being formed by a combination of both mechanisms. However, in nearly all mixed cases homogeneous freezing produced many more ice crystals and therefore dominated the cirrus properties. The dominant nucleation mechanism is defined here as that which generated a higher ice crystal concentration.

Data availability:

In situ data and model output for this study are publically available at https://doi.org/10.3334/ORNLDAAC/2006. ATom aircraft data are publically available at https://doi.org/10.3334/ORNLDAAC/1925.

Code availability:

Code for the CESM model is publically available at http://www.cesm.ucar.edu/models/cesm1.0/. Code for the GEOS model is publically available at https://gmao.gsfc.nasa.gov/GEOS_systems/.

Methods References:

50. Wofsy, S. C. *et al. ATom: Merged Atmospheric Chemistry, Trace Gases, and Aerosols*. https://daac.ornl.gov/cgi-bin/dsviewer.pl?ds_id=1581 (2018) doi:10.3334/ornldaac/1581.
51. Liu, J. *et al.* Representativeness of CO and O3 along ATom Transects Derived from GEOS-5 and GMI-CTM Simulations. *Prep.* (2021).
52. Brock, C. A. *et al.* Aerosol size distributions during the Atmospheric Tomography Mission (ATom): methods, uncertainties, and data products. *Atmos. Meas. Tech.* **12**, 3081–3099 (2019).
53. Williamson, C. *et al.* Fast time response measurements of particle size distributions in the 3–60 nm size range with the nucleation mode aerosol size spectrometer. *Atmos. Meas. Tech.* **11**, 3491–3509 (2018).
54. Kupc, A., Williamson, C., Wagner, N. L., Richardson, M. & Brock, C. A. Modification, calibration, and performance of the Ultra-High Sensitivity Aerosol Spectrometer for particle size distribution and volatility measurements during the Atmospheric Tomography Mission (ATom) airborne campaign. *Atmos. Meas. Tech.* **11**, 369–383 (2018).
55. McNaughton, C. S. *et al.* Results from the DC-8 inlet characterization experiment (DICE): Airborne versus surface sampling of mineral dust and sea salt aerosols. *Aerosol Sci. Technol.* **41**, 136–159 (2007).
56. Thomson, D. S., Schein, M. E. & Murphy, D. M. Particle Analysis by Laser Mass Spectrometry WB-57F Instrument Overview. *Aerosol Sci. Technol.* **33**, 153–169 (2000).
57. Murphy, D. M. *et al.* Single-particle mass spectrometry of tropospheric aerosol particles. *J. Geophys. Res. Atmos.* **111**, D23S3 (2006).
58. Murphy, D. M., Middlebrook, A. M. & Warshawsky, M. Cluster analysis of data from the Particle Analysis by Laser Mass Spectrometry (PALMS) instrument. *Aerosol Sci.*

Technol. **37**, 382–391 (2003).

59. Diskin, G. S., Podolske, J. R., Sachse, G. W. & Slate, T. A. Open-path airborne tunable diode laser hygrometer. *Proc. SPIE* **4817**, 196 (2002).
60. Podolske, J. R. Calibration and data retrieval algorithms for the NASA Langley/Ames Diode Laser Hygrometer for the NASA Transport and Chemical Evolution Over the Pacific (TRACE-P) mission. *J. Geophys. Res.* **108**, 8792 (2003).
61. Rollins, A. W. *et al.* Evaluation of UT/LS hygrometer accuracy by intercomparison during the NASA MACPEX mission. *J. Geophys. Res. Atmos.* **119**, 1915–1935 (2014).
62. Chan, K. R., Dean-Day, J., Bowen, S. W. & Bui, T. P. Turbulence measurements by the DC-8 Meteorological Measurement System. *Geophys. Res. Lett.* **25**, 1355–1358 (1998).
63. Bardeen, C. G., Toon, O. B., Jensen, E. J., Marsh, D. R. & Harvey, V. L. Numerical simulations of the three-dimensional distribution of meteoric dust in the mesosphere and upper stratosphere. *J. Geophys. Res.* **113**, D17202 (2008).
64. Toon, O. B., Turco, R. P., Westphal, D., Malone, R. & Liu, M. A multidimensional nodel for aerosols: Description of computational analogs. *J. Atmos. Sci.* **45**, 2123–2144 (1988).
65. Ginoux, P. *et al.* Sources and distributions of dust aerosols simulated with the GOCART model. *J. Geophys. Res. Atmos.* **106**, 20255–20273 (2001).
66. Su, L. & Toon, O. B. Numerical simulations of Asian dust storms using a coupled climate-aerosol microphysical model. *J. Geophys. Res.* **114**, D14202 (2009).
67. Gillette, D. A. & Passi, R. Modeling dust emission caused by wind erosion. *J. Geophys. Res. Atmos.* **93**, 14233–14242 (1988).
68. Creamean, J. M. *et al.* Colorado air quality impacted by long-range-transported aerosol: A set of case studies during the 2015 Pacific Northwest fires. *Atmos. Chem. Phys.* **16**, 12329–12345 (2016).
69. Tobo, Y. *et al.* Glacially sourced dust as a potentially significant source of ice nucleating particles. *Nat. Geosci.* **12**, 253–258 (2019).
70. Zhang, G. J. & McFarlane, N. A. Sensitivity of climate simulations to the parameterization of cumulus convection in the Canadian climate centre general circulation model. *Atmosphere-Ocean* **33**, 407–446 (1995).
71. Wang, H. *et al.* Sensitivity of remote aerosol distributions to representation of cloud–aerosol interactions in a global climate model. *Geosci. Model Dev.* **6**, 765–782 (2013).
72. Grell, G. A. & Freitas, S. R. A scale and aerosol aware stochastic convective parameterization for weather and air quality modeling. *Atmos. Chem. Phys.* **14**, 5233–5250 (2014).
73. Chin, M. *et al.* Tropospheric Aerosol Optical Thickness from the GOCART Model and Comparisons with Satellite and Sun Photometer Measurements. *J. Atmos. Sci.* **59**, 461–483 (2002).
74. Bian, H. *et al.* Investigation of global particulate nitrate from the AeroCom phase III experiment. *Atmos. Chem. Phys.* **17**, 12911–12940 (2017).
75. Rienecker, M. M. *et al.* The GEOS- 5 data assimilation system: Documentation of versions 5.0.1 and 5.1.0, and 5.2.0 (NASA Tech. Rep.). *Ser. Glob. Model. Data Assim. NASA/TM- 2008- 104606* (2008).
76. Bowman, K. P. Large-scale isentropic mixing properties of the Antarctic polar vortex from analyzed winds. *J. Geophys. Res. Atmos.* **98**, 23013–23027 (1993).
77. Bowman, K. P. & Carrie, G. D. The mean-meridional transport circulation of the troposphere in an idealized GCM. *J. Atmos. Sci.* **59**, 1502–1514 (2002).

78. Spichtinger, P. & Gierens, K. M. Modelling of cirrus clouds – Part 1b: Structuring cirrus clouds by dynamics. *Atmos. Chem. Phys.* **9**, 707–719 (2009).
79. Jensen, E. J., Pfister, L. & Bui, T. P. Physical processes controlling ice concentrations in cold cirrus near the tropical tropopause. *J. Geophys. Res. Atmos.* **117**, (2012).
80. Murphy, D. M. Rare temperature histories and cirrus ice number density in a parcel and a one-dimensional model. *Atmos. Chem. Phys.* **14**, 13013–13022 (2014).
81. Jensen, E. J. *et al.* Physical processes controlling ice concentrations in synoptically forced, midlatitude cirrus. *J. Geophys. Res. Atmos.* **118**, 5348–5360 (2013).
82. Jensen, E. & Pfister, L. Transport and freeze-drying in the tropical tropopause layer. *J. Geophys. Res.* **109**, D02207 (2004).
83. Koop, T., Luo, B., Tsias, A. & Peter, T. Water activity as the determinant for homogeneous ice nucleation in aqueous solutions. *Nature* **406**, 611–614 (2000).
84. DeMott, P. J. Quantitative descriptions of ice formation mechanisms of silver iodide-type aerosols. *Atmos. Res.* **38**, 63–99 (1995).
85. Cziczo, D. J. *et al.* Deactivation of ice nuclei due to atmospherically relevant surface coatings. *Environ. Res. Lett.* (2009) doi:10.1088/1748-9326/4/4/044013.
86. Sullivan, R. C. *et al.* Irreversible loss of ice nucleation active sites in mineral dust particles caused by sulphuric acid condensation. *Atmos. Chem. Phys.* **10**, 11471–11487 (2010).
87. DeMott, P. J., Rogers, D. C. & Kreidenweis, S. M. The susceptibility of ice formation in upper tropospheric clouds to insoluble aerosol components. *J. Geophys. Res. Atmos.* **102**, 19575–19584 (1997).
88. Kärcher, B., Hendricks, J. & Lohmann, U. Physically based parameterization of cirrus cloud formation for use in global atmospheric models. *J. Geophys. Res.* **111**, D01205 (2006).
89. Podglajen, A., Hertzog, A., Plougonven, R. & Legras, B. Lagrangian temperature and vertical velocity fluctuations due to gravity waves in the lower stratosphere. *Geophys. Res. Lett.* **43**, 3543–3553 (2016).
90. Schoeberl, M. R. *et al.* Gravity wave spectra in the lower stratosphere diagnosed from project loon balloon trajectories. *J. Geophys. Res. Atmos.* **122**, 8517–8524 (2017).

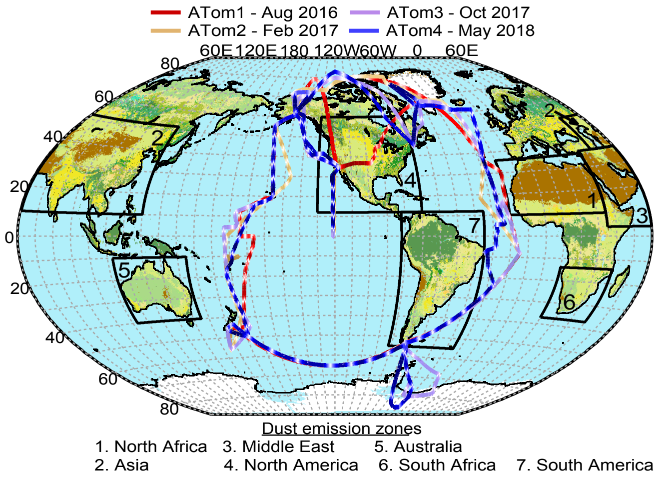
ATom1 - Aug 2016
ATom2 - Feb 2017
ATom3 - Oct 2017
ATom4 - May 2018
60E
120E
180
120W
60W
0
60E
80
60
40
20
0
20
40
60
80
1
2
3
4
5
6
7
Dust emission zones
1. North Africa
2. Asia
3. Middle East
4. North America
5. Australia
6. South Africa
7. South America

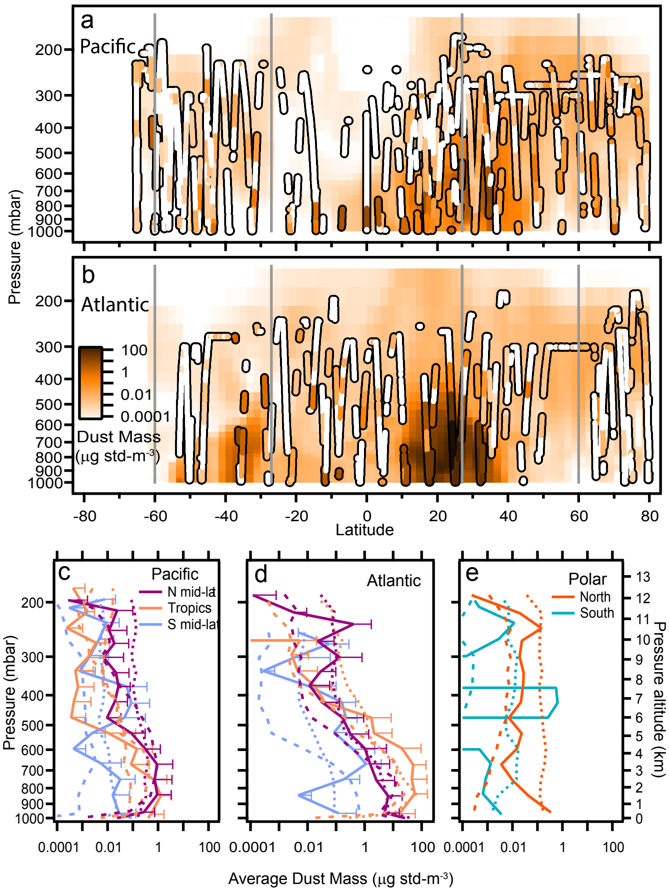
a
Pacific
b
Atlantic
Pressure (mbar)
200
300
400
500
600
700
800
900
1000
100
1
0.01
0.0001
Dust Mass
(µg std-m-3)
-80
-60
-40
-20
0
20
40
60
80
Latitude
c
Pacific
N mid-la
Tropics
S mid-la
d
Atlantic
e
Polar
North
South
Pressure altitude (km)
13
12
11
10
9
8
7
6
5
4
3
2
1
0
0.0001
0.01
1
100
Average Dust Mass (µg std-m-3)

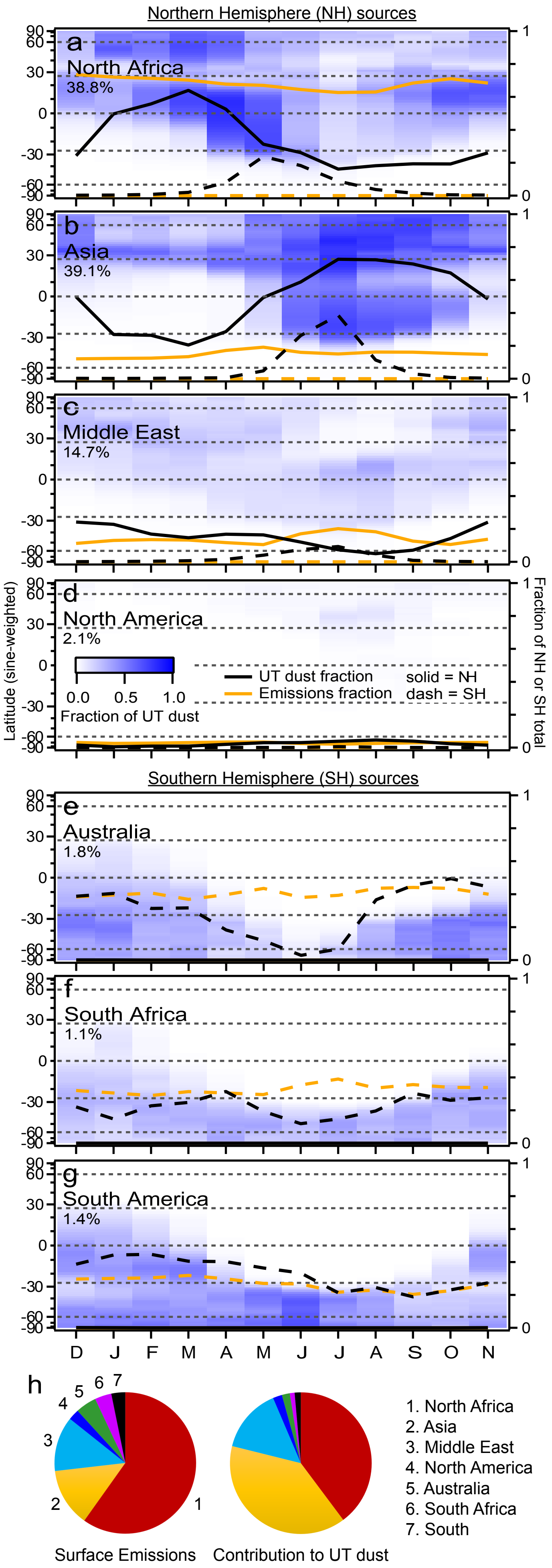
Northern Hemisphere (NH) sources
a
North Africa
38.8%
b
Asia
39.1%
c
Middle East
14.7%
d
North America
2.1%
0.0
0.5
1.0
Fraction of UT dust
UT dust fraction
Emissions fraction
solid = NH
dash = SH
Latitude (sine-weighted)
Fraction of NH or SH total
90
60
30
0
-30
-60
-90
1
0
Southern Hemisphere (SH) sources
e
Australia
1.8%
f
South Africa
1.1%
g
South America
1.4%
D
J
F
M
A
M
J
J
A
S
O
N
h
1
2
3
4
5
6
7
Surface Emissions
Contribution to UT dust
1. North Africa
2. Asia
3. Middle East
4. North America
5. Australia
6. South Africa
7. South

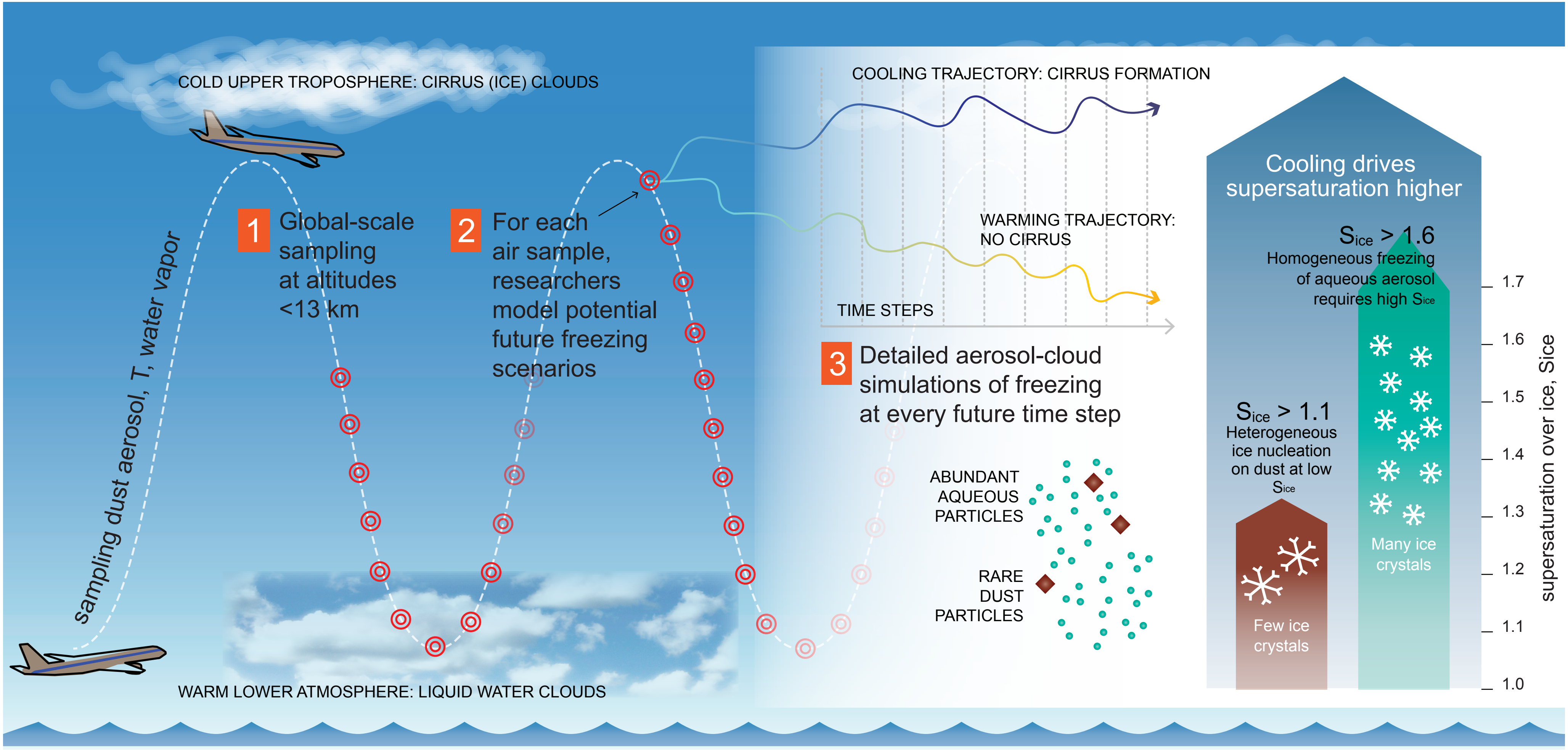
COLD UPPER TROPOSPHERE: CIRRUS (ICE) CLOUDS
sampling dust aerosol, T, water vapor
1 Global-scale sampling at altitudes <13 km
2 For each air sample, researchers model potential future freezing scenarios
COOLING TRAJECTORY: CIRRUS FORMATION
WARMING TRAJECTORY: NO CIRRUS
TIME STEPS
3 Detailed aerosol-cloud simulations of freezing at every future time step
ABUNDANT AQUEOUS PARTICLES
RARE DUST PARTICLES
Cooling drives supersaturation higher
S_{ice} > 1.6
Homogeneous freezing of aqueous aerosol requires high S_{ice}
S_{ice} > 1.1
Heterogeneous ice nucleation on dust at low S_{ice}
Few ice crystals
Many ice crystals
1.7
1.6
1.5
1.4
1.3
1.2
1.1
1.0
supersaturation over ice, Sice
WARM LOWER ATMOSPHERE: LIQUID WATER CLOUDS

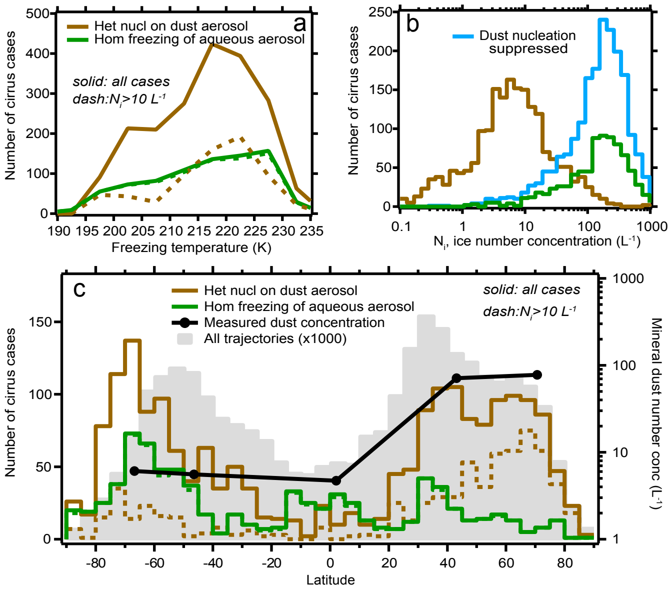
a
Het nucl on dust aerosol
Hom freezing of aqueous aerosol
solid: all cases
dash:N_i>10 L^{-1}
Number of cirrus cases
0
100
200
300
400
500
190 195 200 205 210 215 220 225 230 235
Freezing temperature (K)
b
Dust nucleation suppressed
Number of cirrus cases
0
50
100
150
200
250
0.1
1
10
100
1000
N_i, ice number concentration (L^{-1})
c
Het nucl on dust aerosol
Hom freezing of aqueous aerosol
Measured dust concentration
All trajectories (x1000)
solid: all cases
dash:N_i>10 L^{-1}
Number of cirrus cases
0
50
100
150
-80
-60
-40
-20
0
20
40
60
80
Latitude
Mineral dust number conc (L^{-1})
1
10
100
1000